JGR Atmospheres

RESEARCH ARTICLE
10.1029/2024JD042371

Anthropogenic Carbon Monoxide Emissions During 2014–2020 in China Constrained by In Situ Ground Observations

Mengwei Jia[1], Fei Jiang[1,2,3], Nikolaos Evangeliou[4], Sabine Eckhardt[4], Andreas Stohl[5], Xin Huang[6], Yang Shen[1], Shuzhuang Feng[1], Wei He[1], Jun Wang[1], Hengmao Wang[1], Mousong Wu[1], Weimin Ju[1], and Aijun Ding[6]

[1]Jiangsu Provincial Key Laboratory of Geographic Information Science and Technology, International Institute for Earth System Science, Nanjing University, Nanjing, China, [2]Jiangsu Center for Collaborative Innovation in Geographical Information Resource Development and Application, Nanjing, China, [3]Frontiers Science Center for Critical Earth Material Cycling, Nanjing University, Nanjing, China, [4]Department of Atmospheric and Climate Research, NILU, Kjeller, Norway, [5]Department of Meteorology and Geophysics, University of Vienna, Vienna, Austria, [6]Joint International Research Laboratory of Atmospheric and Earth System Sciences, School of Atmospheric Sciences, Nanjing University, Nanjing, China

Abstract China has been actively reducing anthropogenic air pollutant emissions over the past decade and is about to embark on the next phase of air quality management. Carbon monoxide (CO) is an ideal indicator of primary pollutants from combustion sources. A comprehensive assessment of the current situation of anthropogenic CO emissions can inform the implementation of future reduction policies. This work aims to determine the changes of anthropogenic CO emissions in mainland China from 2014 to 2020 at 0.2° × 0.2° spatial resolution. Hourly CO observations from over 1,600 national control sites were combined with Lagrangian dispersion modeling and multisectoral emission inventories in a Bayesian inversion framework, to determine monthly CO emissions. From 2014 to 2020, the average annual anthropogenic CO emission in mainland China was 473.6 ± 117.2 Tg a^{-1}, which is 2.5 times higher than the prior emission. Northwest China stands out as the most underestimated region with a relative difference of an astonishing 6.3 times between prior and posterior emissions. The emissions generally decreased by 32.0% from 2014 to 2020, but with a clear rebound in 2017 and 2018, and Yunnan in the southwest and Xinjiang in the northwest are the most pronounced rebound provinces. Optimizing the management of direct emissions in the future requires not only focusing on key urban agglomerations but also strengthening controls in remote provinces.

Plain Language Summary Over the past decade, China has implemented some of the strictest air pollution control measures in the world, leading to major changes in its industrial structure, energy production structure, energy intensity, and emissions intensity. Anthropogenic CO emissions are an ideal indicator of pollution from combustion sources, but it is challenging to get an accurate and timely picture of how these emissions have changed in China. To illustrate the anthropogenic CO emissions and trends in China, we constrained the monthly CO emissions from 2014 to 2020 using in situ ground hourly observations from over 1,600 monitoring sites. Our findings reveal that the average annual anthropogenic CO emissions during this period were 473.6 ± 117.2 Tg per year. While emissions decreased by 32.0% overall from 2014 to 2020, there was a noticeable rebound in 2017 and 2018. This suggests that China's anthropogenic CO emissions are much higher than previously estimated, with a trend characterized by significant fluctuations.

Key Points:

- The anthropogenic CO emissions in China from 2014 to 2020 are constrained by in situ ground observations
- The average annual anthropogenic CO emission was 473.6 ± 117.2 Tg a^{-1}, which is 2.5 times higher than the emission inventory
- The emissions generally decreased by 32.0%, but with a clear rebound in 2017 and 2018

Supporting Information:

Supporting Information may be found in the online version of this article.

Correspondence to:

F. Jiang,
jiangf@nju.edu.cn

Citation:

Jia, M., Jiang, F., Evangeliou, N., Eckhardt, S., Stohl, A., Huang, X., et al. (2025). Anthropogenic carbon monoxide emissions during 2014–2020 in China constrained by in situ ground observations. *Journal of Geophysical Research: Atmospheres*, *130*, e2024JD042371. https://doi.org/10.1029/2024JD042371

Received 31 AUG 2024
Accepted 4 MAY 2025

Author Contributions:

Conceptualization: Aijun Ding
Data curation: Sabine Eckhardt, Xin Huang
Funding acquisition: Weimin Ju
Investigation: Yang Shen, Shuzhuang Feng
Methodology: Nikolaos Evangeliou
Project administration: Jun Wang, Hengmao Wang
Resources: Xin Huang
Software: Shuzhuang Feng
Supervision: Fei Jiang, Andreas Stohl
Validation: Yang Shen
Visualization: Mengwei Jia
Writing – original draft: Mengwei Jia
Writing – review & editing: Mengwei Jia, Fei Jiang, Nikolaos Evangeliou, Sabine Eckhardt, Andreas Stohl, Wei He, Mousong Wu

1. Introduction

CO is one of the most important air pollutants, which is mainly produced by the incomplete combustion of fossil fuels or biofuels and biomass burning (Hosely et al., 2018; van der Werf et al., 2017). Anthropogenic emissions from vehicles, industrial processes, and residential heating systems govern the CO concentrations in the atmosphere above China (Zheng et al., 2019). The main sink of CO is the reaction with hydroxide radicals (OH), leading to a global average atmospheric lifetime of CO of 1–3 months (Seinfeld & Pandis, 2016). The predominance of direct anthropogenic emissions, relatively well-known sink rates, and relatively long lifetime of 1–3 months make CO an ideal indicator of primary emissions from combustion sources (Barret et al., 2016; Ding et al., 2013; Jia, Huang, et al., 2021; Sauvage et al., 2017). Therefore, it is necessary to investigate the CO emissions, trends, and underlying drivers.

China has implemented several stringent air pollution control measures, such as the "Action Plan for Air Pollution Prevention and Control" and the "Three-year Action Plan on Defending the Blue Sky", to mitigate severe air pollution (Ding et al., 2019). In November 2023, China just released the "Action Plan for Continuous Improvement of Air Quality", suggesting that more strict air quality management policies will still be implemented in the coming years. These effective policies reformed the industrial structure, energy production structure, energy intensity, and emissions intensity (Cai et al., 2018; Guan et al., 2018; Jia et al., 2023; Zheng et al., 2018). However, due to the large uncertainty and time lag, we cannot get an accurate and timely picture of changes in China's CO anthropogenic emissions from "bottom-up" inventories (Feng, Jiang, Wu, et al., 2020; Li et al., 2017; Saikawa et al., 2017). Previous research has also uncovered that the CO emission bias is considered the principal cause of the underestimation in CO simulation models (Gaubert et al., 2020; Kong et al., 2020; Stein et al., 2014).

To enhance the precision of CO anthropogenic emissions, in situ observations or space-based remotely sensed measurements have been assimilated to constrain emissions, named "top-down" methods (Miyazaki et al., 2015; Qu et al., 2022; Thompson et al., 2016). The tropospheric total column retrieved from the spaceborne measurements of pollution in the troposphere instrument (MOPITT, Deeter et al., 2017) is the most commonly used space-based remotely sensed measurements. However, the coverage of space-based remotely sensed measurements maybe inadequate due to clouds, atmospheric pollution, and high surface albedo, and the sensitivity of column concentrations to surface CO fluxes is not well understood. Therefore, space-based remotely sensed measurements are mostly used to invert global CO emissions (Gaubert et al., 2020; Jiang et al., 2017; Yin et al., 2015; Zheng et al., 2019). Another observation is in situ measurements, which are sufficient in China and verified to enable relative high-resolution (<1°) inversion of CO emissions. Feng, Jiang, Wu, et al. (2020) have inverted China's total CO emissions in China in December 2013 and 2017 based on the monitoring network established by the Ministry of Ecology and Environment (MEE). Kong et al. (2023) inverted the long-term emissions of several air pollutants, including CO, by assimilating surface observations from MEE as well. However, all these studies inverted total CO budgets rather than quantifying anthropogenic emissions. Besides, the spatial and temporal characteristics of China's anthropogenic CO emissions during the implementation of the two important air quality policy measures remain vague.

In a previous study performed by our group, we explored the high-resolution CO emission changes in the Fenwei Plain, China. In this study, we aim to provide accurate top-down estimates and characteristics of mainland China's CO anthropogenic emissions for the period covering the implementation of two important air quality policies. We constrain the monthly CO emission in a resolution of $0.2° \times 0.2°$ by in situ hourly ground observations from over 1,600 national control sites in the entire mainland China. Then, we compare the inversion results with bottom-up emission inventories and confirm their reliability. Finally, we investigate the spatiotemporal characteristics of anthropogenic CO emissions from 2014 to 2020.

2. Materials and Methods

2.1. Inversion Method

In this study, we use the Lagrangian-Bayesian inversion framework of FLEXINVERT to estimate the monthly CO emissions in mainland China based on in situ ground measurements. The Lagrangian-Bayesian inversion framework, FLEXINVERT (Thompson and Stohl, 2014), has been developed to infer emissions at variable resolutions from regional to intercontinental scales (Evangeliou et al., 2018; Jia, Huang, et al., 2021, Jia, Evangeliou, et al., 2021; Thompson et al., 2015). It also has been often used previously for source emission optimization of fossil fuel combustion products, greenhouse gases, and other trace gases, such as CO, BC, CH_4, $CHCl_3$, and SF_6, in many regions with different land uses and emission characteristics (Brunner et al., 2017; Fang et al., 2019; Jia et al., 2023; Thompson et al., 2017).

FLEXINVERT is based on source-receptor relationships calculated by FLEXPART and Bayesian statistical principles to optimize the prior emission fluxes within a given range of uncertainty to match the atmospheric observations. Assuming that CO transport is a linear problem, the matrix operator can be expressed as Equation 1 as follows:

$$y^{obs} = Hx + \varepsilon \quad (1)$$

where y^{obs} is a vector of the measured CO concentrations, H is the SRR matrix, x is an emissions matrix, and ϵ is a vector of the combined model and observation errors.

Based on the Bayesian statistical optimization method (Thompson and Stohl, 2014), we can construct the cost function of Equation 2, in which x_b is the prior emission, B is the prior error covariance matrix, and R is the observation error covariance matrix, which includes measurement errors, transport model errors, and observation representation errors.

$$J(x) = \frac{1}{2}(x - x_b)^T B^{-1}(x - x_b) + \frac{1}{2}\left(Hx - y^{obs}\right)^T R^{-1}\left(Hx - y^{obs}\right) \quad (2)$$

By minimizing the cost function Equation 2, we could obtain the posterior emissions of CO as Equation 3 as follows:

$$x = x_b + \left(H^T R^{-1} H + B^{-1}\right)^{-1} H^T R^{-1}\left(y^{obs} - H_{x_b}\right) \quad (3)$$

The posterior error covariance matrix, A, is equivalent to the inverse of the second derivative of the cost function.

$$A = (J'')^{-1} = B - BH^T\left(HBH^T + R\right)^{-1} HB \quad (4)$$

2.2. Atmospheric Transport

The FLEXPART version 10.1 was employed to calculate the source (CO emissions)-receptor (a measurement site here) relationship (SRR) (Lai and Chen, 2007; Seibert and Frank, 2004; Stohl, 1998) every 3 hr during the daytime. The SRR quantified the receptor sensitivity to surface emissions (Ding et al., 2009; Jia, Huang, et al., 2021; Kljun et al., 2002; Stohl et al., 2003) (Figure 1a). We quantified SRRs in a global domain with a resolution of 1° × 1° over mainland China with a variable resolution grid. Because the information content of the observation was not large enough everywhere to constrain the emissions at a uniform fine resolution and to improve the computational efficiency of the inversion, we adopted a variable resolution inversion grid with a resolution ranging from 0.2° × 0.2°–1.6° × 1.6° inside the nested domain from 66°E to 136°E and 15°N–55°N (Figure 1b and Figure S1 in Supporting Information S1). With this method, the spatial resolution was kept higher in areas with a high density of observing stations, leading to high SRR values (Thompson and Stohl, 2014) and degraded in regions with low SRR values.

Therefore, the transport operator H in Equation 2 is constructed from three atmospheric transport components for each receptor: (a) H^{nest}: transport of fluxes within a nested domain, (b) H^{out}: transport of fluxes outside the nested domain, and (c) H^{bg}: contribution of mixing ratios at the time and location when the back trajectories terminate. Similarly, the vector x in Equation 2 is composed of f^{nest}, fluxes inside the domain; f^{out}, fluxes inside the domain; and y^{bg}, initial mixing ratios taken from the output of a global model. By defining the concentration of CO over 10 days using the global model's CO simulations, we can ensure that our inversion results are not affected by changes in CO lifetime. The following is the modeling equation for CO concentrations:

$$y^{mod} = H^{nest} f^{nest} + H^{out} f^{out} + H^{bg} y^{bg} \quad (5)$$

The meteorological input data consisted of operational meteorological analyses from the European Centre for Medium-Range Weather Forecasts (ECMWF). While the typical lifetime of CO in the troposphere is 1–2 months, we only ran FLEXPART back from the measurement sites for 10 days (Stohl et al., 2003). This period is sufficiently long to capture the emissions from China almost fully. However, in order to make the model results comparable with the measurements, it is necessary to add a "background" CO concentration during the CO simulations. The Copernicus Atmosphere Monitoring Service (CAMS) global atmospheric composition reanalysis monthly average CO concentration field (Innes et al., 2019) from 2014 to 2020 was utilized as the background (i.e., y^{bg} in Equation 5), namely the CO concentrations at the endpoints of the 10-day back trajectories. These values were combined with the concentration resulting from emission contributions during the last 10 days as the simulated concentrations. This method was previously employed in studies by Stohl (2006), Ding et al. (2009, 2013), and Jia et al. (2021a, 2023). Furthermore, the loss of CO due to its reaction with the hydroxyl

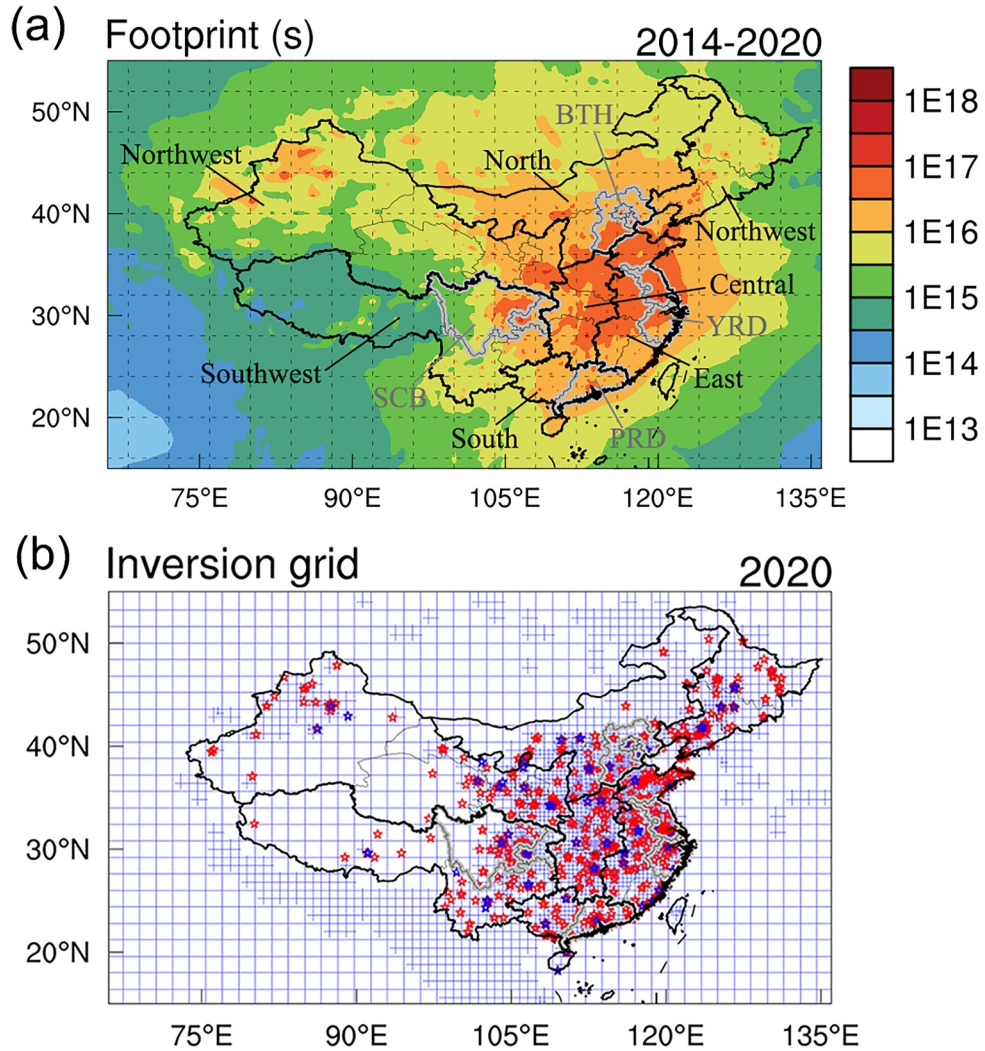

Figure 1. (a) SRR (in seconds) accumulated over all sites and time steps between 2014 and 2020. (b) Inversion grid with variable resolution inside the nested model domain in 2020. Red stars and blue stars are inversion sites and independent sites, respectively.

radical (OH) during the 10-day simulation period was also taken into account. Considering the seasonal differences in reaction rates, we utilized the monthly average OH field simulated by the Goddard Earth Observing System-Chem (GEOS-Chem) model, which has a spatial resolution of 4° × 5° (Bey et al., 2001).

2.3. Observation Data and Errors

Hourly CO measurements from about 1,600 stations across China from 2014 to 2020 were used, which are taken from a comprehensive monitoring network established by the MEE. The maximum number of available sites was 1,632 in 2019 (Figure S2 in Supporting Information S1). Atmospheric CO monitoring and data quality control are conducted according to the national meteorological standard QX/T 273-2015 (2015) and the national environmental protection standards HJ 818-2018 (2018). The instrument type is a conversational air quality monitoring system, and the monitoring method is infrared gas filter correlation, with commonly used instruments such as Thermo Instruments. The monitoring instruments are operated continuously throughout the year at a temperature of 25°C ± 5°C and a relative humidity of less than 80% and are regularly cleaned and calibrated. Observations are from the data platform of NEE (https://air.cnemc.cn:18007/, last access: 01/06/2025).

Considering that most of the national control sites are concentrated in urban areas with often only small differences in CO concentrations, it would be inefficient to invert all these observations individually. Therefore,

before the inversion calculation, the station observations were thinned according to the distance from each other. The specific algorithm is the same as described in Jia et al. (2023). This method reduces the number of stations by 25%–37%, that is, still keeping more than 1,000 sites, and preserving most of the information contained in the full station data set. Meanwhile, depending on the year, 7.7%–11.2% of the sites were kept outside the inversion and named independent sites, as the blue sites in Figure 1b. This allowed us to verify the inversion results with independent data.

The observation error covariance matrix (R) specifies the error structure of the observation vector y^{obs}, including measurement errors, transport model errors, and observation representation errors. The root sum of the squares of these three errors is defined as the observation error covariance matrix (Jia et al., 2023) as follows:

$$\sigma^2 = \sigma^2_{meas} + \sigma^2_{trans} + \sigma^2_{repr} \quad (6)$$

For the measurement error, we refer to two studies: (a) Kim et al. (2008) analyzed the measurement errors of long-term CO observations in China, which was 22 ppb. (b) Feng, Jiang, Wu, et al. (2020) used the same CO observational data in China and found an average measurement error of about 8 ppb. Hence, the measurement error is assumed to be the average of these two studies, which is about 15 ppb (~0.02 mg m^{-3}). The transport model error depends on the model, meteorological input data, resolution, and location, which is extremely challenging to quantify, so we do not specifically include an estimate for it (Thompson and Stohl, 2014). Due to the complexities associated with simulating the nighttime atmospheric boundary layer, when emissions often accumulate in a shallow layer of uncertain depth, only daytime measurements (0900–1800 LST) were considered in order to reduce transport errors. For the observation representation error, we adopted the averaged 1-sigma standard deviation that was averaged for hourly daytime measurements at all inversion sites (Jia et al., 2023; Thompson et al., 2015), which is 0.2 mg m^{-3}. In summary, we took one decimal place of the total observation error, which is 0.2 mg m^{-3}.

The reliability of the model can be assessed by the reduced chi-square value (χ^2), which corresponds to the value of the cost function at its optimum—equivalent to the weighted sum of squares divided by the number of observations. Ideally, χ^2 equals 1, indicating that the posterior solution is within the specified uncertainty. The choice of error covariance matrix hypothesis in Equation 2 directly influences the resulting χ^2 value. Thompson et al. (2015) reported χ^2 values ranging from 2.6 to 3.9 in their methane emission inversion experiment for East Asia (2000–2011). In this study, the specific values for the prior error covariance matrix and the observation error covariance matrix have been validated in our previous inversion study of CO emissions in the Fenwei Plain, China (Jia et al., 2023). We evaluated the configurations of the prior error covariance matrix and the observation error covariance matrix using χ^2 and obtained values slightly below 1, ranging between 0.5 and 0.8. These results suggest that the posterior solutions are consistent with the specified uncertainties, further supporting the reliability of our model.

2.4. Prior Emissions and Uncertainties

In this study, the definition of "anthropogenic CO" in this article includes not only emissions from fossil fuels but also from biofuels, wood burning, and some other sources related to human activities. Our inversion method ensures that our definition of anthropogenic CO is consistently applied throughout the models and emission inventories. The prior emissions consist of three bottom-up emission inventories, the Multi-resolution Emission Inventory model for Climate and air pollution research (MEIC), the Global Fire Emissions Database (GFED), and the Peking University (PKU).

The MEIC emission inventory solely represents anthropogenic emissions, which was considered as the optimal prior emission data set for CO in mainland China (Li et al., 2017; Zheng et al., 2018). We used MEIC version 1.4 from 2014 to 2020, which has a spatial resolution of 0.25° × 0.25° and encompasses monthly emission data (Figure S3a in Supporting Information S1), with a maximum value of 851.7 Mg km^{-2} a^{-1}. The MEIC inventory classifies anthropogenic emissions into five sectors: industry, power, transport, residential, and agriculture, with the agricultural sector assumed to have negligible CO emissions. For the remaining four sectors, MEIC incorporates not only fossil fuel consumption but also biomass fuel consumption for residential use, drawing on data from tens of thousands of household surveys (Peng et al., 2019).

The GFED emission inventory was implemented to estimate nonanthropogenic CO emissions (van der Werf et al., 2017) (Figure S3b in Supporting Information S1). We used GFED version 4.1 throughout the period of 2014–2020, which also has a spatial resolution of 0.25° × 0.25°. The GFED emission inventory combines satellite information on fire activity and vegetation productivity to estimate gridded monthly burned area and fire emissions, which encompasses the monthly emissions and fractional contributions of many different fire types, including savanna, grassland fires, shrubland fires, boreal forest fires, temperate forest fires, deforestation, degradation, peatland fires, and agricultural waste burning.

Considering the clear distinction between anthropogenic and nonanthropogenic sources in both MEIC and GFED inventories, we add MEIC and GFED as the prior emission in the nested domain (i.e., f^{nest} in Equation 5), and multiply the total posterior emission by the proportion of the anthropogenic emission in model grid cell as given by MEIC and GFED to derive anthropogenic emissions (Jiang et al., 2017; Yin et al., 2015; Zheng et al., 2018, 2019). Statistically, the average annual share of China's wildfire emissions (GFED) in the total prior emissions (GFED and MEIC) from 2014 to 2020 is 14.8%.

For regions outside mainland China, the global CO emission inventory from the Peking University (PKU) was used (i.e., f^{out} in Equation 5), which has a spatial resolution of 0.1° × 0.1° and a temporal resolution of 1 month (Wang et al., 2014; Zhong et al., 2017). PKU contains not only anthropogenic emission sectors, including agriculture, energy production, industry, transportation, residential, and commercial, but also deforestation and wildfire emissions.

The uncertainty of anthropogenic CO emission inventories in China has been well assessed. Zhang et al. (2009), Kurokawa et al. (2013), and Zhao et al. (2013) estimated anthropogenic emissions of CO in China with uncertainties of ±70%, ±86%, and −18%–42%, respectively. However, the uncertainty of the Chinese CO fire emission inventory is still not clarified. Considering the average annual share of China's wildfire emissions in the total prior emissions is less than 15%, the uncertainties of these emissions are not considered in our simulations. Referring to previous studies, our prior flux uncertainty was set to an intermediate value of 70% (Zhang et al., 2009) in China. Correlations between uncertainties were considered using an exponential decay function with a scale length of 250 km on land and a timescale over 30 days. The uncertainty of national and regional posterior emissions was evaluated by the sensitivity to perturbed prior emission inventories. Different prior emissions have the potential to lead to large discrepancies in flux estimates. Therefore, we perturb our prior emissions using PKU-CO emission inventory (Figure S4 in Supporting Information S1). The formulas for standard deviation (SD) and relative standard deviation (RSD) are as follows:

$$\mathrm{SD} = \sqrt{\frac{\sum_{i=1}^{n}(x_i - \overline{x})^2}{n}} \tag{7}$$

$$\mathrm{RSD} = \frac{\mathrm{SD}}{\overline{x}} \tag{8}$$

3. Results and Discussions

3.1. Evaluation Against In Situ Observations

In order to examine the changes in CO emissions during and after the implementation of China's strongest air pollution control measures to date, we performed monthly inversions of CO emissions across mainland China from 2014 to 2020. Before analyzing the emission characteristics, it is necessary to further validate our results and to assess the improvement of the emission estimates based on all inversion observations. Therefore, we simulated the CO concentrations at all sites using the prior and posterior emissions, and then compared them with the observations. Monthly mean biases (MBs) between simulated and observed CO concentrations are counted at all inversion sites and independent sites (Figure 2).

To validate the results, we implemented an independent testing protocol by reserving a subset of observation sites that were excluded from the inversion process. The testing protocol was based on two key criteria. First, we examined whether significant discrepancies existed in CO concentration simulations between independent sites and inversion sites when driven by posterior emissions. Second, we assessed whether posterior emission-driven simulations demonstrated substantially improved accuracy over prior emission-driven simulations at independent

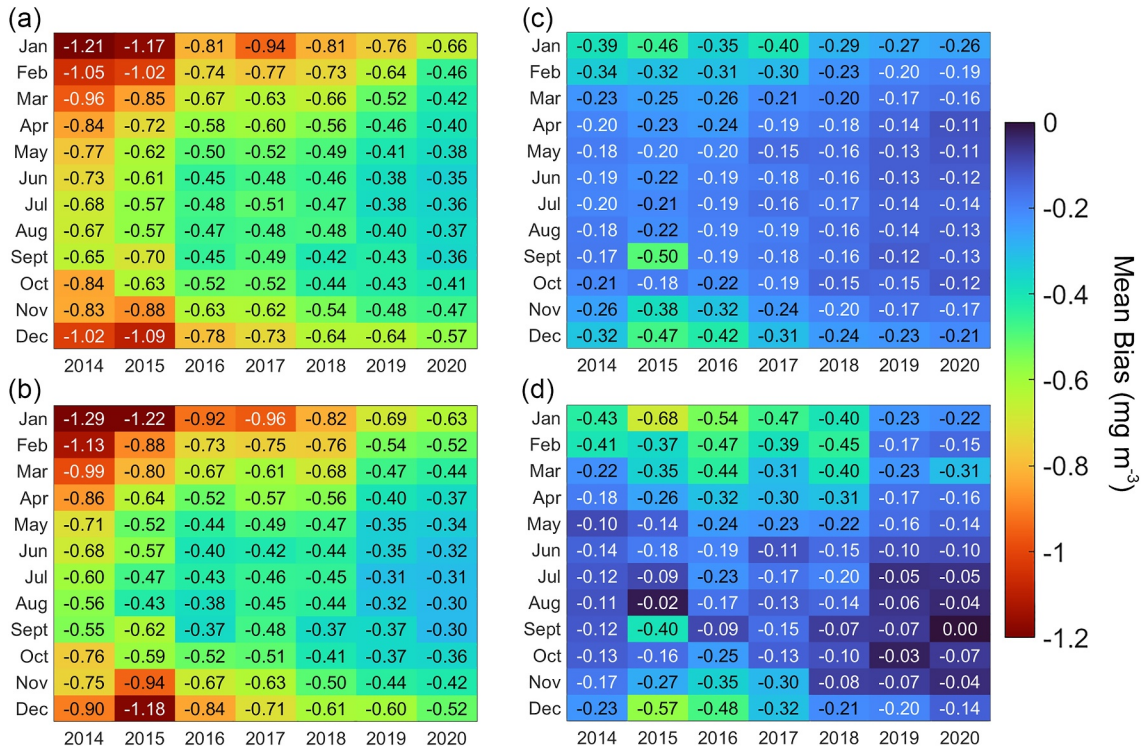

Figure 2. Heat maps of monthly MBs between simulated and observed CO concentrations at inversion sites and independent sites from 2014 to 2020 (mg m^{-3}): (a) the prior emissions at inversion sites, (b) the prior emissions at independent sites, (c) the posterior emissions at inversion sites, and (d) the posterior emissions at independent sites.

sites. As illustrated in Figure 2, our analysis of MBs between simulated and observed CO concentrations revealed two important findings: (a) The MBs of posterior emission-driven CO simulations showed no significant variation between independent and inversion sites (Figures 2c and 2d). (b) The MBs of posterior emission-driven simulations at independent sites were markedly smaller than those of prior emission-driven simulations (Figures 2b and 2d). These consistent results provide robust confirmation of our inversion results' reliability.

The average MBs of posterior emissions are just −0.22 mg m^{-3} at both inversion sites and independent sites, while the average MBs of the prior simulated concentrations reach −0.62 and −0.59 mg m^{-3} at inversion sites and independent sites (Figure 2), which implied that the biases of the posterior simulated concentrations are reduced by ∼64% compared to the biases of the prior simulated concentrations. This is strong evidence that the posterior emission error is significantly reduced compared to the prior emission.

For the prior emissions, the MBs are characterized by yearly decreases, with the average annual MBs for the prior simulated concentrations in 2020 being only 50.9% of that in 2014, which implied the improvement in the accuracy of the prior emissions (Figures 2a and 2b). Besides, it is obvious that the MBs for the prior simulated concentrations are larger in winter than in other seasons. Due to winter heating, China's CO emissions are more diverse in winter, which may lead to larger uncertainty of the prior emissions. In addition, there is a clear geographical distribution of winter heating in China, with large amounts of fossil fuels being burned for centralized heating in winter in the region north of the Qinling-Huaihe River (∼34°N). From the spatial distribution of MBs (Figures 3a–3c and Figure S5 in Supporting Information S1), they are indeed significantly higher in northern China than in southern China.

For the posterior emissions, the mean bias decreases significantly after the observational constraints (Figures 2c and 2d). The north-south differences in the posterior simulated concentrations of MBs are also significantly weaker (Figures 3d–3f). But what cannot be ignored is similar to the prior simulated concentration; the MBs for the posterior simulated concentration decrease annually, and are higher in winter than in summer. Referring to previous studies, we assume that the prior emission uncertainty of a fixed value during 2014–2020, as we mentioned in Section 2.4, leads to larger uncertainties of the posterior emissions in winter than in other seasons.

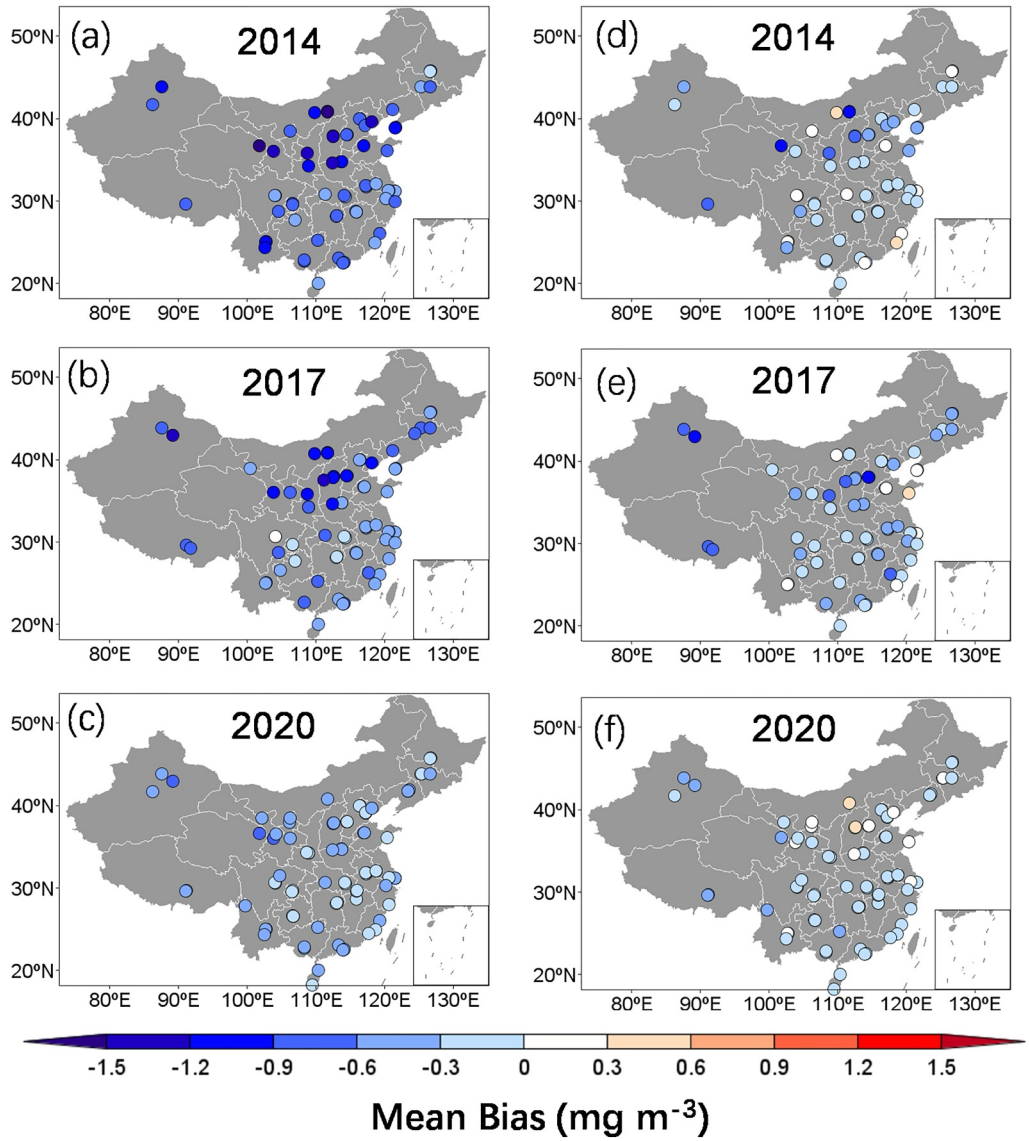

Figure 3. MBs between the prior and posterior simulated concentrations and observations at all independent sites in 2014, 2017, and 2020. (a–c) MBs of prior simulated concentrations and observations. (d–f) MBs of posterior simulated concentrations and observations.

The posterior emissions are still underestimated, especially for 2014–2018, which may lead to an underestimation of the reduction in emissions in our calculations.

Apart from MB, we also compared root mean square errors (RMSEs) and normalized mean errors (NMEs) in all inversion sites over the representative months (Figure S6 in Supporting Information S1). RMSEs and NMEs of the posterior emission simulation results showed a decrease, and the correlation coefficient (r) demonstrated an increase. All NMEs fall below 0.50 mg m^{-3}, with a minimum of 0.36 mg m^{-3} for the posterior emission simulations. RMSEs and NMEs decreased by 26.0% and 35.9%, respectively, on average at the inversion site from 2014 to 2020, which also confirms the significant improvement in the accuracy of the posterior emissions compared to the prior emissions.

3.2. Averaged Anthropogenic CO Emissions From 2014 to 2020

The prior emission, posterior emission, and their differences in anthropogenic CO emissions averaged over the period from 2014 to 2020 are depicted in Figure 4. The average annual anthropogenic CO posterior emissions for

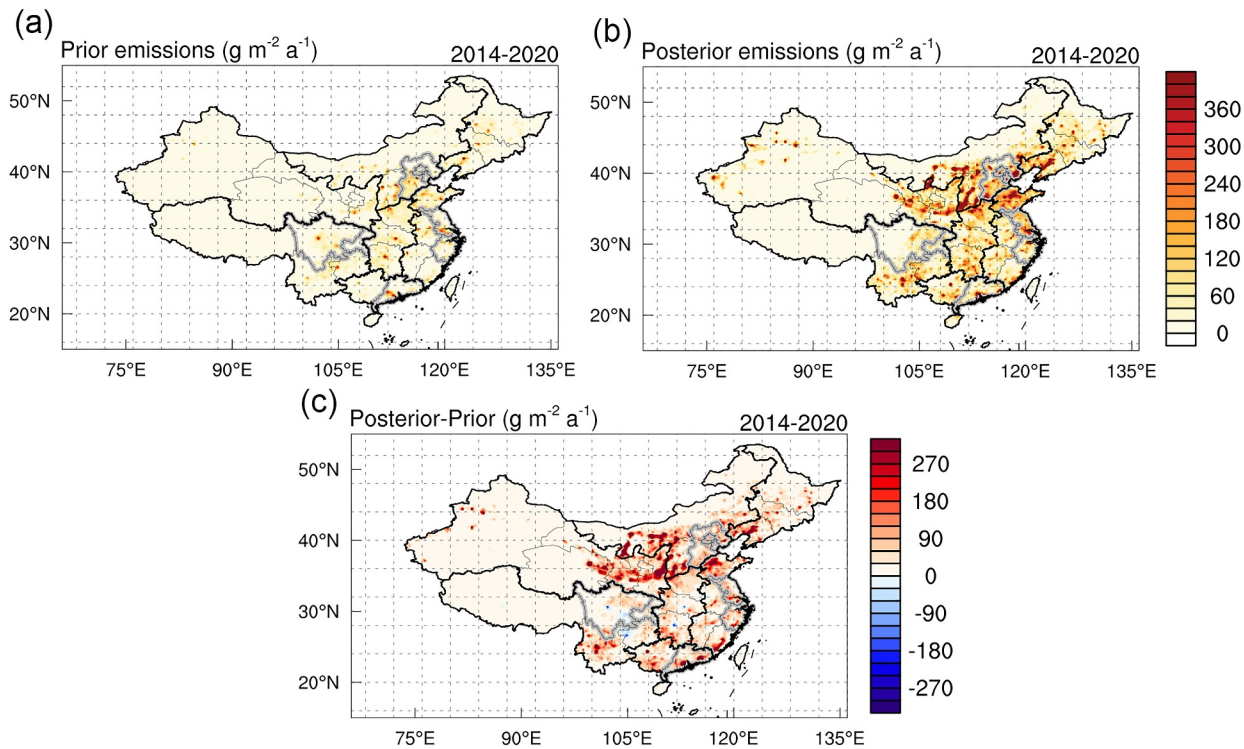

Figure 4. Average anthropogenic CO emissions in China from 2014 to 2020: (a) prior emissions, (b) posterior emissions, and (c) the difference between them.

mainland China amounted to 473.6 (±117.2) Tg a^{-1}. In terms of the difference between prior and posterior emissions, it can be observed that the prior emissions are generally lower than the posterior emissions in most regions. This means that the emission inventories underestimate the real emissions. To quantify the degree of underestimation, we define the relative difference as the following equation:

$$\text{relative difference} = \frac{x_{\text{pos}} - x_{\text{pri}}}{x_{\text{pri}}} \tag{9}$$

in which x_{pos} and x_{pri} are regional aggregations of posterior and prior emission, respectively. As shown in Figure 5, the national relative difference is 2.5 averaging from 2014 to 2020, with values greater than 1.0 in all regions.

In general, the Chinese mainland can be classified into seven geographic regions: northwest China, Southwest China, Northeast China, Central China, East China, south China, and North China (Figure 1a). The top three geographic regions in terms of total anthropogenic emissions are North China, East China, and northwest China, which account for more than half of the national emissions. The relative differences between posterior and prior emissions are 6.3, 1.9, 2.2, 1.6, 3.2, 2.9, and 1.7 for northwest, Southwest, Northeast, Central, south, North, and East China, respectively. The vast size of the northwest region makes it difficult to fully account for the location and intensity of anthropogenic activities using only bottom-up methods, which could lead to a significant underestimation of the prior emissions.

The Beijing-Tianjin-Hebei (BTH) region in North China, the Yangtze River Delta (YRD) in East China, the Pearl River Delta (PRD) in south China, and the Sichuan Basin (SCB) in Southwest China are currently the most developed large urban agglomerations in China, leading the rest of the country in terms of economy, population, and transportation infrastructure (National Bureau of Statistics, 2020). The average anthropogenic emissions between 2014 and 2020 are 33.7 ± 6.5 Tg a^{-1} in BTH, 27.2 ± 5.6 Tg a^{-1} in YRD, 19.8 ± 4.1 Tg a^{-1} in PRD, and 17.7 ± 3.2 Tg a^{-1} in SCB. The relative differences against the a priori emissions are 1.2, 1.4, 2.8, and 1.2 for BTH, YRD, PRD, and SCB, respectively. Comparing the ratios of these urban agglomerations to the geographic regions they belong to, we find that the relative differences for the urban agglomerations are smaller than the regional values. For instance, the relative difference for BTH (1.2) is smaller than that for the North China (2.9). This

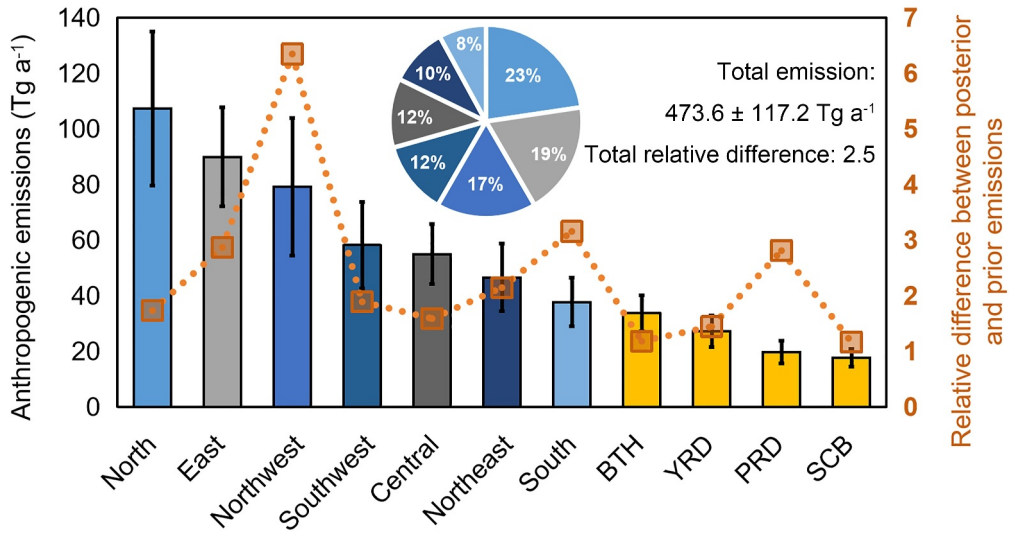

Figure 5. Average posterior anthropogenic CO emissions and relative difference to the prior emissions. The bars represent the emissions and uncertainties, and the pie charts are the proportions of emissions with the color corresponding to the bars. The orange line shows a relative difference between posterior and prior emissions.

suggests that the prior emission errors may be larger in less developed regions. Besides, in terms of spatial distribution, the high CO emissions are not just found in large urban agglomerations but are concentrated in energy-intensive industrial areas.

3.3. Interannual Variations of Anthropogenic CO Emissions

We further explore the annual anthropogenic CO emissions from 2014 to 2020. Figure 6 illustrates the annual prior and posterior CO emissions for mainland China as a whole and the relative differences between posterior and prior emissions for the seven regions separately. The prior emissions in mainland China show a modest continuous decrease between 2014 and 2020 (Figure 6a). Conversely, the posterior emissions demonstrate noticeable interannual fluctuations superimposed on a negative overall trend, characterized by a strong decrease from 2014 to 2016, an increase in 2017 and 2018, and a further decline in the years 2019–2020. This

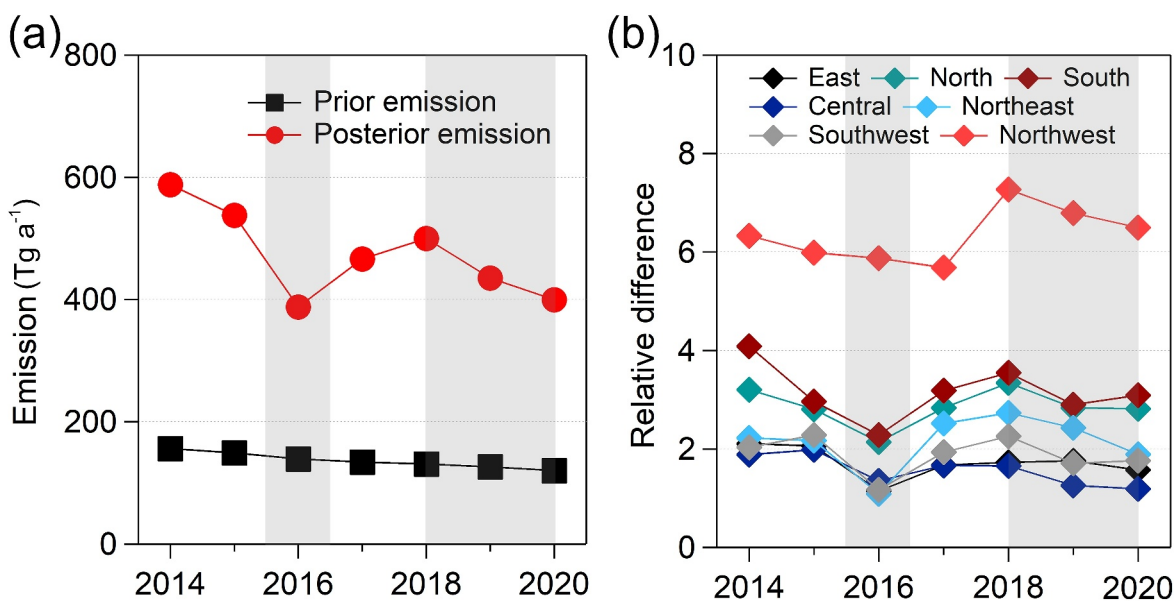

Figure 6. (a) Annual prior (black) and posterior (red) anthropogenic CO emissions from 2014 to 2020 and (b) their relative differences for the seven geographic regions.

characterization is quite different from the trend of CO concentrations, which decreased continuously from 2014 to 2020 in mainland China and was illustrated in our previous research (Jia et al., 2023). This is mainly not only because CO concentration is affected by CO emissions but also because the meteorological field can greatly influence the spatial distribution of CO. The highest emissions occurred in 2014, with posterior emissions of 587.9 Tg a−¹, while the lowest took place in 2016, at 388.1 Tg a−¹. It is worth noting that the emission in 2020 (399.7 Tg a^{-1}) is lower than that in 2019, which maybe related to the disruption of anthropogenic activities by the COVID-19 lockdown in 2020 (Feng, Jiang, Wang, et al., 2020; Jia, Evangeliou, et al., 2021; Mao et al., 2024). For the lockdown period, which is January and February 2020, CO emissions were recorded at 31.9 and 31.4 Tg, respectively. These values were not only significantly lower than emissions during the same period in previous years but also lower than summer emissions of the same year, marking the first occurrence of such a phenomenon since 2014.

We utilized the sectoral emission ratios from the MEIC inventory to estimate sector-wise emissions (Table S1 in Supporting Information S1). From a sectoral perspective, in 2014, the industry sector was the largest emitting sector, followed by residential. By 2020, due to the rapid decline in CO emissions from the industry sector, industrial emissions had fallen below residential emissions. Regarding emission reduction rates, the industry sector exhibited the highest average decline rate of −15.1 Tg a^{-2}, followed by the residential sector (−10.2 Tg a^{-2}), and the transport sector (6.1 Tg a^{-2}). While the power sector had the lowest CO emissions overall, it showed a slight increase in emissions. In February 2020, sectoral analysis based on MEIC data shows a sharp decline in the transport sector's contribution, dropping to 7.0%, which is half of its 2019 share (13.9%), with emissions decreasing by 60.6%. This aligns with the restrictions on nationwide human mobility. The industrial sector also shows a significant reduction, with its share falling from 25.4% in 2019 to 20.9% in 2020, indicating substantial constraints on industrial production. In absolute terms, industrial emissions in February 2020 were 6.6 Tg, and only 64.7% of the emissions in February 2019 (10.2 Tg). Although the residential sector's share increased from 57.5% to 68.8% due to the lockdown, its total emissions still declined by 6.3%. Meanwhile, the power sector's contribution remained relatively stable, likely because power generation continued to operate during COVID-19.

Figure 6b shows the relative differences between annual posterior and prior emissions in the seven geographic regions. The northwest has the largest relative difference in posterior emissions of all years. The highest value was 7.3 in 2018. The relative difference in the northwest declined to the lowest in 2017. However, in other regions, the relative differences are much lower in 2016 than in 2017. This means that except for the northwest, most of the regions in mainland China experienced a rebound in CO emissions in 2017. It is also remarkable that relative increases in the northwest are larger for the period 2018–2020 than before, suggesting that posterior emissions increases strongly in those years. Similar results were obtained by Feng et al. (2024) who inverted the emissions of fossil fuel carbon dioxide (CO_2) in China, which is homologous to anthropogenic CO, and found that fossil fuel CO_2 emissions in northwest China are most significantly underestimated.

Figure 7 illustrates the national and regional mean anthropogenic CO emission trends of both prior and posterior emissions from 2014 to 2020. It can be observed that anthropogenic CO emissions in most regions of China exhibited a consistent decline. We find an annual change rate of −23.5 Tg a^{-2} for the posterior emissions, but merely −5.8 Tg a^{-2} for the prior emissions. Considering the annual reductions in the underestimation of posterior emissions, the annual change rate is likely to be lower than −23.5 Tg a^{-2}. Compared to 2014, the national anthropogenic CO emissions in 2020 decreased by at least 32.0% for posterior emissions, but only 23.0% for prior emissions. Distinguished spatial disparities exist in the patterns of CO emission fluctuations. The slow decline in CO emissions in northwest and Northeast China is largely attributable to rising CO emissions in Xinjiang, Xizang, and Heilongjiang provinces. In terms of emission rates (Figure S7 in Supporting Information S1), Kashgar Prefecture, Hotan Prefecture, and Ili Kazakh Autonomous Prefecture in western Xinjiang showed significant increases, even to a maximum of 123.2 Mg km^{-2} a^{-2}. Furthermore, a sharp increase in the CO emission rate also occurred near the geographical boundary between the provinces of Sichuan and Yunnan, which is up to 153.6 Mg km^{-2} a^{-2}.

From the above analysis, it can be inferred that national anthropogenic CO emissions have not been decreasing continuously since the implementation of the "Action Plan for Air Pollution Prevention and Control" (2013). To gain a better understanding of the response of CO emissions to the Action Plan, we determined the annual total anthropogenic CO emissions for each province. Figure 8 shows the annual changes in total anthropogenic CO emissions by provincial administrative regions. We found that 19 of the 31 provincial administrative regions in

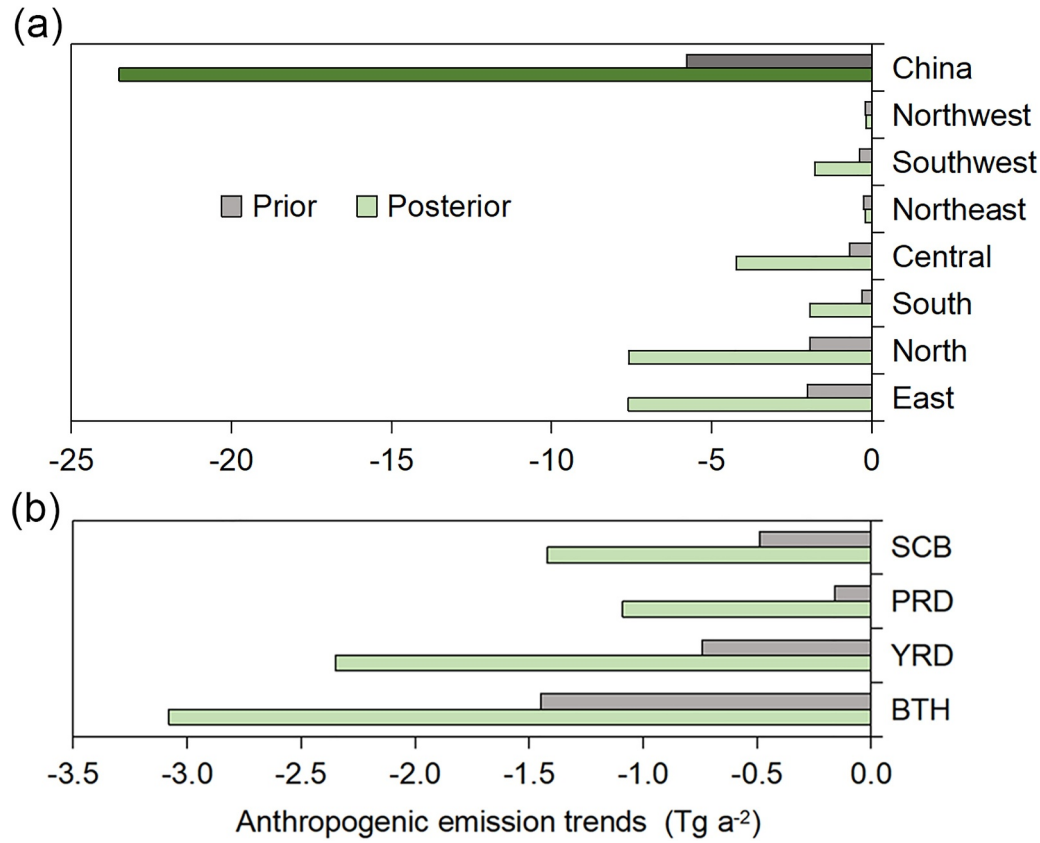

Figure 7. National and regional CO emission trends over the period 2014–2020 for both prior (gray) and posterior (green) estimates for China as a whole and seven geographic regions (a) and four urban agglomerations (b).

mainland China showed a decrease in CO emissions in 2015, with the most pronounced decrease (10.8 Tg) occurring in Shanxi in North China. However, there were still some provinces where emissions increased, with the most significant rise in Sichuan province. Anthropogenic emissions of CO continued to decline in 2016, with all provincial administrative regions experiencing a downward trend, especially in Inner Mongolia, Hebei, Yunnan, and Shandong, which all decreased by more than 10 Tg, with the largest reduction of 14.1 Tg in Inner Mongolia. A broad rebound in total anthropogenic CO emissions occurred in 2017 and 2018, rising in 23 provincial administrative regions, with Yunnan and Inner Mongolia increasing their emissions by more than 11.0 Tg in 2017 and Xinjiang by more than 6.9 Tg for these 2 years. Consistent with the trend in CO anthropogenic emissions, coal consumption rebounded in 2017 (Figure S8 in Supporting Information S1). CO anthropogenic emissions dropped again in most provinces in 2019 and 2020. While coal consumption still increased in 2019, its share of total energy consumption was 8.1% lower and the share of nonfossil fuels was 4% higher than 2014 (National Bureau of Statistics, 2021). The energy consumption transition by improved CO emission control measures maybe one of the reasons for the decline in anthropogenic CO emissions after 2019. The anthropogenic emissions in Xinjiang, Liaoning, Zhejiang, Jiangsu, and Anhui provinces were unusually active in 2019 when the emissions were declining in most provinces.

3.4. Discussions

Although we have confirmed the reliability of the inversion results, further discussions of China's CO emissions are still warranted due to the substantial underestimation of the emission inventory. Besides the large uncertainties of CO emissions in China as we mentioned in Section 2.4, almost all studies with top-down approaches have reported an underestimation of anthropogenic CO emissions in bottom-up inventories for China (Feng, Jiang, Wu, et al., 2020; Jia et al., 2023; Kopacz et al., 2010; Pan et al., 2014; Tanimoto et al., 2008; Yumimoto et al., 2014; Zheng et al., 2019). For MEIC specifically, Feng, Jiang, Wu, et al. (2020) reported that it underestimates the CO emissions in China, with a 186% and a 178% increase of the posterior emission in December 2013 and 2017,

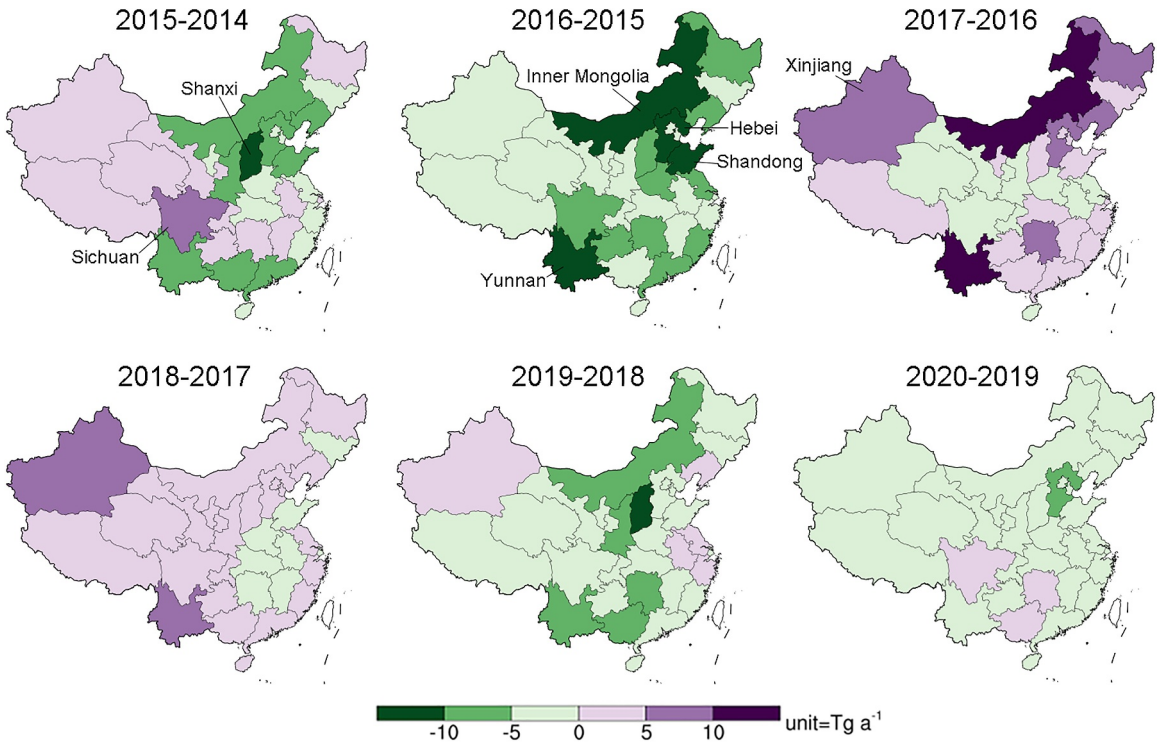

Figure 8. Annual changes in CO anthropogenic emissions by provinces (unit: Tg a^{-1}).

respectively, and found that the underestimation is largest in the northwest, with 600% and 376% increases of posterior emissions in December 2013 and 2017, respectively. In addition to the large uncertainties in the existing CO emission inventories, we find that while MEIC investigated rural residential solid fuel consumption of raw coal, briquettes, wood, and crop residues in the form of a questionnaire (Peng et al., 2019), it does not incorporate emissions from livestock excrement burning. However, this miss only leads to a minor underestimation of approximately 0.6% of total biomass burning emissions in China (Zhou et al., 2017).

We compared previous top-down inversion estimates of CO emissions in China from several published works with our results (Table 1). Feng, Jiang, Wu, et al. (2020) and Kong et al. (2023) constrained China's CO emission budget using in situ observations in a higher resolution ($\leqq$0.25°), which are similar to our inversion. Feng, Jiang, Wu, et al. (2020) inverted China's CO emissions in December 2013 and 2017 based on the WRF-CMAQ model and the ensemble Kalman filter algorithm, and concluded that the CO emissions in December 2017 were 43.0 Tg. Our estimate for December 2017 is 39.4 Tg. Despite the slight difference in the prior emissions (15.5 Tg for Feng, Jiang, Wu, et al. (2020) and 16.2 Tg for us), both this study and the inversion results of Feng, Jiang, Wu, et al. (2020) concluded that the prior emissions significantly underestimated the CO emissions in China. Kong et al. (2023) inverted China's CO emissions from 2013 to 2020 based on the nested air quality prediction modeling system (NAQPMS) model and an ensemble of Kalman filters. They also concluded the underestimation of the CO emission inventory, with the estimation being more than twice the amount in previous inventories. Other works constrained CO emissions based on satellite data in a lower resolution ($\geq$0.95°). Zheng et al. (2019) inverted the average China's anthropogenic emissions of CO to 162.2 Tg a^{-1} at a resolution of 3.75° × 1.9° from 2010 to 2017 using the Measurements Of Pollution In The Troposphere (MOPITT) instrument. Combined with the relative trend, the average annual emissions from 2014 to 2017 were estimated to be ~154 Tg a^{-1}. Our inversion is about 3.2 times larger than this number. Jiang et al. (2017) estimated regional CO emissions in China except for western China, which are approximately equal to China's emissions except for the provinces of Xinjiang and Xizang provinces. They concluded that the regional CO emissions in 2014 and 2015 were 169.0 and 154.9 Tg a^{-1}, respectively, which were much lower than our estimation for China except Xinjiang and Xizang provinces in 2014 (638.2 Tg a^{-1}) and 2015 (631.1 Tg a^{-1}). Similarly, the CO emission estimates of Gaubert et al. (2020) are also much lower than those of this study. Satellite-derived CO column concentrations integrate three-dimensional

Table 1
Inversion-Based Estimates of China's CO Emissions and Trends Since the Implementation of the "Action Plan for Air Pollution Prevention and Control"

	Sources	Average emissions (Tg a^{-1})	Relative change (% a^{-1})	Time period	Resolution	Observation	Transport model
Jiang et al. (2017)	ALL	169.0	−8.3	2014	4° × 5°	Satellite	GEOS-Chem
		154.9		2015			
Gaubert et al. (2020)	ALL	Central China 91.2	–	5/2016	1.25° × 0.95°	Satellite	CAM-Chem
		North China 58.8					
Feng, Jiang, Wu, et al. (2020)	ALL	624.2	−4.3	12/2013	0.25° × 0.25°	Surface	WRF-CMAQ
		516.4		12/2017			
Kong et al. (2023)	ALL	Year 2015	−7.7	2015–2020	15 km × 15 km	Surface	NAQPMS
		465.4					
This study	ALL	538.3	−4.5	2014–2020	0.2° × 0.2°	Surface	FLEXPART
Zheng et al. (2019)	Anthropogenic	162.2	−2.2	2010–2017	3.75° × 1.9°	Satellite	LMDz-SACS
This study	Anthropogenic	473.6	−5.3	2014–2020	0.2° × 0.2°	Surface	FLEXPART

meteorological transport processes throughout the entire vertical profile and are influenced by aerosol and cloud disturbances. As a result, satellite data are less sensitive to CO emissions than ground-based observations. Many studies have demonstrated that satellite observation in high-emission areas may underestimate CO concentrations, especially in urban areas and industrial zones (Deeter et al., 2017; Streets et al., 2013; Worden et al., 2013). Gaubert et al. (2020) and Zheng et al. (2019) also found that while assimilating MOPITT satellite data substantially improves model simulations of CO concentrations in China, the values remain lower than those from aircraft measurements and in situ observations. Furthermore, MOPITT's 3-day revisit cycle results in limited temporal resolution, which contrasts sharply with our continuous hourly CO concentration measurements obtained from in situ sites. These studies have fully confirmed that even top-down inversion methods have large discrepancies in estimating CO emissions in China. Besides, we compared the inversion results with the Emissions Database for Global Atmospheric Research (EDGAR) (Crippa et al., 2024) (Figure S8 in Supporting Information S1). The average CO emissions from EDGAR from 2014 to 2020 were only 122.4 Tg a^{-1}, which is 80.3 Tg a^{-1} lower than the prior emissions. The relative difference indicates that the posterior emissions are 3.4 times higher than those of EDGAR, highlighting that the underestimation in bottom-up inventories is not an isolated case. Additionally, China's CO emissions are confirmed much higher than India's emissions. In 2020, India's CO emissions are still even less than one-tenth of China's emissions (Sahu et al., 2024).

In addition to anthropogenic sources, the simulation of CO can also be influenced by CO sinks through hydroxyl radical (OH) reactions, and chemical production through the oxidation of methane (CH_4) and nonmethane volatile organic compounds (NMVOCs) (Jiang et al., 2017; Müller et al., 2018; Zheng et al., 2019). We do not consider the interannual variation of CO emissions in the impact of chemical production, mainly because CO chemical production has demonstrated remarkable stability over multiyear timescales and constitutes a substantially smaller fraction than primary CO in China. As corroborated by Zheng et al. (2019) for the 2000–2017 period, while global methane oxidation showed a slight increasing trend (3.0 ± 0.4 TgCO a^{-2}), this was effectively counterbalanced by decreasing NMVOCs oxidation yields (−3.6 ± 1.5 TgCO a^{-2}). Dasari et al. (2022) revealed that rapidly developing regions exhibit primary CO contributions significantly exceeding the global average (55% ± 5%), with South Asia reaching 79% ± 4%. China's anthropogenic CO emissions demonstrate an even higher predominance of primary sources than South Asia (Zheng et al., 2019), indicating that secondary CO contributes a markedly smaller proportion relative to combined anthropogenic and biomass burning emissions. Besides, CO chemical production maybe related to El Niño, but their relationship is quite complex. On the one hand, during strong El Niño episodes (e.g., 2015–2016), drought conditions in South/Southeast Asia intensify biomass burning activities, leading to increased NMVOCs emissions and subsequent CO increases. On the other hand, elevated temperatures and humidity variations during such events suppress OH radical concentrations, thereby reducing oxidation rates of methane and NMVOCs, ultimately decreasing CO production (Roemer and van den Hout, 1992). Future research could benefit from quantifying how El Niño and other yearly climatic variations affect interannual changes in CO emission sources.

Unlike previous CO emission inventories, this study argues that China's CO emissions rebounded in 2017 after a significant decline in 2016. The decline in CO emissions from 2015 to 2016 coincides with trends in energy consumption in the National Statistical Yearbook (2021) (Figure S8 in Supporting Information S1), where consumption of fossil fuels, especially coal, a relatively unclean energy source, declined in both 2015 and 2016, by 48.8 and 23.6 million tons (Mt) of standard coal equivalent (SCE), respectively, while consumption of nonfossil fuels (primary electricity and other energy sources) rose sharply in both years, especially in 2016, reaching 57.8 Mt SCE. The decline in national coal consumption and the rise in nonfossil fuel consumption may contribute to the decline in anthropogenic CO emissions in 2015 and 2016. CO_2, which is homologous to anthropogenic CO, is able to characterize anthropogenic activity levels to some extent. Shi et al. (2022) estimated China's CO_2 emissions from 2013 to 2020 with and without clean air action measures, and it showed even with clean action measures; China's CO_2 increased significantly in 2017. Many emission data sets also show a significant rebound in CO_2 emissions in 2017 compared to 2016, such as British Petroleum (BP), Global Carbon Budget (GCB), Carbon Dioxide Information Analysis Center (CDIAC), the U.S. Energy Information Administration (EIA), Multi-resolution Emission Inventory for China (MEIC), and national sectoral emissions of China Emission Accounts and Data sets (CEADs) (Shan et al., 2020).

The uncertainty of national and regional inversion results was evaluated in Table S1 of Supporting Information S1, which presents the mean gridded SDs and RSDs of the two different posterior emissions from 2014 to 2020, resulting from different emission inventories. The mean SD is 117.2 Tg a^{-1}, and the mean RSD is 24.7% in mainland China, and the regions with the largest SD and RSD are North China and Northwest China, respectively. The RSDs of the four major urban agglomerations are relatively consistent, ranging from 18% to 21%.

4. Conclusions

In this study, we investigated the variation in anthropogenic CO emissions in China in recent years (2014–2020). A Lagrangian particle dispersion model (FLEXPART) and a Bayesian inversion framework (FLEXINVERT) were employed in this study to provide monthly top-down CO emissions at a resolution of 0.2° across the country. Hourly CO observations from approximately 1,600 in situ stations in mainland China were utilized from 2014 to 2020.

We conclude that the average annual anthropogenic CO emissions in China from 2014 to 2020 were 473.6 ± 117.2 Tg a^{-1}. North, East, and northwest China are the three regions with the largest anthropogenic emissions. The prior emission from the MEIC bottom-up inventory underestimates anthropogenic emissions widely. The total relative difference between posterior and prior emissions is 2.5, while the northwest reached an astonishing 6.3.

The national anthropogenic CO emissions decreased by at least 32.0% (at a rate of −23.5 Tg a^{-2}) from 2014 to 2020, which dropped from 2014 to 2016, increased in 2017 and 2018, and then declined again in 2019 and 2020. More than 20 provinces showed an increase in CO anthropogenic emissions in 2017 and 2018. Yunnan in the southwest and Xinjiang in the northwest were the most pronounced rebound provinces in 2017 and 2018, respectively, and anthropogenic emissions in the Xinjiang Province were unusually active in 2019 when the emissions were declining in most provinces.

China has achieved remarkable results in emissions reduction in recent years, but it is still crucial to be wary of updated emission changes. Optimizing the management of direct emissions in the future requires not only focusing on key urban agglomerations but also strengthening controls in remote provinces such as Yunnan and Xinjiang provinces.

Data Availability Statement

FLEXINVERT is available online at https://flexinvert.nilu.no/. The following data are uploaded to Zenodo.org (Jia, 2024): (a) all emission data, including total CO prior and posterior emissions, anthropogenic emissions, and wildfire emissions (as netCDF), (b) the posterior simulated CO concentrations (as txt), and (c) total CO emissions, anthropogenic emissions, and wildfire emissions in seven regions (as CSV).

Acknowledgments
The work was funded by the National Natural Science Foundation of China (Grant 42377102), the National Key R&D Program of China (Grant 2023YFB3907404), Jiangsu Provincial Science Fund for Distinguished Young Scholars (Grant BK20231530) and Environmental Protection Science and Technology Program of Fujian Province (Grant 2023R003). We would like to thank the Ministry of Ecology and Environment of the People's Republic of China for making the hourly surface CO concentration observations available (https://air.cnemc.cn:18007/), and the ECMWF for providing the operational meteorological analyses (https://www.ecmwf.int/en/forecasts/dataset/operational-archive). We also thank the MEIC team (http://www.meicmodel.org/), the PKU team (http://inventory.pku.edu.cn/), and the GFED team (https://www.globalfiredata.org/) for providing the CO emission inventory. Additionally, we are also grateful to the High-Performance Computing Center (HPCC) of Nanjing University for doing the numerical calculations on its blade cluster system.

References

Barret, B., Sauvage, B., Bennouna, Y., & Le Flochmoen, E. (2016). Upper-tropospheric CO and O_3 budget during the Asian summer monsoon. *Atmospheric Chemistry and Physics*, *16*(14), 9129–9147. https://doi.org/10.5194/acp-16-9129-2016

Bey, I., Jacob, D. J., Yantosca, R. M., Logan, J. A., Field, B. D., Fiore, A. M., et al. (2001). Global modeling of tropospheric chemistry with assimilated meteorology: Model description and evaluation. *Journal of Geophysical Research*, *106*(D19), 23073–23095. https://doi.org/10.1029/2001JD000807

Brunner, D., Arnold, T., Henne, S., Manning, A., Thompson, R. L., Maione, M., et al. (2017). Comparison of four inverse modelling systems applied to the estimation of HFC-125, HFC-134a, and SF_6 emissions over Europe. *Atmospheric Chemistry and Physics*, *17*, 10651–10674. https://doi.org/10.5194/acp-17-10651-2017

Cai, B., Wang, X., Huang, G., Wang, J., Cao, D., Baetz, B. W., et al. (2018). Spatiotemporal changes of China's carbon emissions. *Geophysical Research Letters*, *45*(16), 8536–8546. https://doi.org/10.1029/2018GL079564

Crippa, M., Guizzardi, D., Pagani, F., Banja, M., Muntean, M., Schaaf, E., et al. (2024). *GHG emissions of all world countries*. Publications Office of the European Union, Luxembourg, 2024. https://doi.org/10.2760/4002897,JRC138862

Dasari, S., Andersson, A., Popa, M. E., Rckmann, T., Holmstrand, H., Budhavant, K., & Gustafsson, Ö. (2022). Observational evidence of large contribution from primary sources for carbon monoxide in the south Asian outflow. *Environmental Science & Technology*, *56*(1), 165–174. https://doi.org/10.1021/acs.est.1c05486

Deeter, M. N., Edwards, D. P., Francis, G. L., Gille, J. C., Martínez-Alonso, S., Worden, H. M., & Sweeney, C. (2017). A climate-scale satellite record for carbon monoxide: The MOPITT version 7 product. *Atmospheric Measurement Techniques*, *10*, 2533–2555. https://doi.org/10.5194/amt-10-2533-2017

Ding, A., Huang, X., Nie, W., Chi, X., Xu, Z., Zheng, L., et al. (2019). Significant reduction of $PM_{2.5}$ in eastern China due to regional-scale emission control: Evidence from SORPES in 2011–2018. *Atmospheric Chemistry and Physics*, *19*(18), 11791–11801. https://doi.org/10.5194/acp-19-11791-2019

Ding, A., Wang, T., & Fu, C. (2013). Transport characteristics and origins of carbon monoxide and ozone in Hong Kong, South China. *Journal of Geophysical Research: Atmospheres*, *118*(16), 9475–9488. https://doi.org/10.1002/jgrd.50714

Ding, A., Wang, T., Xue, L., Gao, J., Stohl, A., Lei, H., et al. (2009). Transport of north China air pollution by midlatitude cyclones: Case study of aircraft measurements in summer 2007. *Journal of Geophysical Research*, *114*(D8), D08304. https://doi.org/10.1029/2008JD011023

Evangeliou, N., Thompson, L. R., Eckhardt, S., & Stohl, A. (2018). Top-down estimates of black carbon emissions at high latitudes using an atmospheric transport model and a Bayesian inversion framework. *Atmospheric Chemistry and Physics*, *18*(20), 15307–15327. https://doi.org/10.5194/acp-18-15307-2018

Fang, X. K., Park, S., Saito, T., Tunnicliffe, R., Ganesan, A. L., Rigby, M., et al. (2019). Rapid increase in ozone-depleting chloroform emissions from China. *Nature Geoscience*, *12*(2), 89–93. https://doi.org/10.1038/s41561-018-0278-2

Feng, S., Jiang, F., Wang, H., Wang, H., He, W., Liu, Y., et al. (2024). China's fossil fuel CO_2 emissions estimated using surface observations of coemitted NO_2. *Environmental Science & Technology*, *58*(19), 8299–8312. https://doi.org/10.1021/acs.est.3c07756

Feng, S., Jiang, F., Wang, H., Wang, H., Ju, W., Shen, Y., et al. (2020). NO_x emission changes over China during the COVID-19 epidemic inferred from surface NO_2 observations. *Geophysical Research Letters*, *47*(19), e2020GL090080. https://doi.org/10.1029/2020GL090080

Feng, S., Jiang, F., Wu, Z., Wang, H., Ju, W., & Wang, H. (2020). CO emissions inferred from surface CO observations over China in December 2013 and 2017. *Journal of Geophysical Research*, *124*(7). https://doi.org/10.1029/2019JD031808

Gaubert, B., Emmons, L. K., Raeder, K., Tilmes, S., Miyazaki, K., Arellano Jr, A. F., et al. (2020). Correcting model biases of CO in East Asia: Impact on oxidant distributions during KORUS-AQ. *Atmospheric Chemistry and Physics*, *20*(23), 14617–14647. https://doi.org/10.5194/acp-20-14617-2020

Guan, D., Meng, J., Reiner, D. M., Zhang, N., Shan, Y. L., Mi, Z. F., et al. (2018). Structural decline in China's CO_2 emissions through transitions in industry and energy systems. *Nature Geoscience*, *11*(8), 551–555. https://doi.org/10.1038/s41561-018-0161-1

Hoesly, R. M., Smith, S. J., Feng, L., Klimont, Z., JanssensMaenhout, G., Pitkanen, T., et al. (2018). Historical (1750–2014) anthropogenic emissions of reactive gases and aerosols from the Community Emissions Data System (CEDS). *Geoscientific Model Development*, *11*(1), 369–408. https://doi.org/10.5194/gmd-11-369-2018

Inness, A., Ades, M., Agustí-Panareda, A., Barré, J., Benedictow, A., Blechschmidt, A.-M., et al. (2019). The CAMS reanalysis of atmospheric composition. *Atmospheric Chemistry and Physics*, *19*(6), 3515–3556. https://doi.org/10.5194/acp-19-3515-2019

Jia, M. (2024). Anthropogenic carbon monoxide emissions during 2014–2020 in China constrained by in situ observations [Dataset]. *Zenodo*. https://doi.org/10.5281/zenodo.13623164

Jia, M., Evangeliou, N., Eckhardt, S., Huang, X., Gao, J., Ding, A., & Stohl, A. (2021). Black carbon emission reduction due to COVID-19 lockdown in China. *Geophysical Research Letters*, *48*(8), e2021GL093243. https://doi.org/10.1029/2021GL093243

Jia, M., Huang, X., Ding, K., Liu, Q., Zhou, D., & Ding, A. (2021). Impact of data assimilation and aerosol radiation interaction on Lagrangian particle dispersion modelling. *Atmospheric Environment*, *247*, 118179. https://doi.org/10.1016/j.atmosenv.2020.118179

Jia, M., Jiang, F., Evangeliou, N., Eckhardt, S., Huang, X., Ding, A., & Stohl, A. (2023). Rapid decline of carbon monoxide emissions in the Fenwei Plain in China during the three-year Action Plan on defending the blue sky. *Journal of Environmental Management*, *337*, 117735. https://doi.org/10.1016/j.jenvman.2023.117735

Jiang, Z., Worden, J. R., Worden, H., Deeter, M., Jones, D. B. A., Arellano, A. F., & Henze, D. K. (2017). A 15-year record of CO emissions constrained by MOPITT CO observations. *Atmospheric Chemistry and Physics*, *17*(7), 4565–4583. https://doi.org/10.5194/acp-17-4565-2017

Kim, H. S., Tans, P. P., & Novelli, P. C. (2008). On the regional background levels of carbon monoxide observed in East Asia during 1991–2004. *Air Quality, Atmosphere & Health*, *1*, 37–44. https://doi.org/10.1007/s11869-008-0001-3

Kljun, N., Rotach, M. W., & Schmid, H. P. (2002). A three-dimensional backward Lagrangian footprint model for a wide range of boundary-layer stratifications. *Boundary-Layer Meteorology*, *103*(2), 205–226. https://doi.org/10.1023/A:1014556300021

Kong, L., Tang, X., Wang, Z., Zhu, J., Li, J., Wu, H., et al. (2023). Changes of air pollutant emissions in China during two clean air action periods derived from the newly developed Inversed Emission Inventory for Chinese Air Quality (CAQIEI). *Earth System Science Data Discussions*, 1–47. https://doi.org/10.5194/essd-2023-477

Kong, L., Tang, X., Zhu, J., Wang, Z., Fu, J. S., Wang, X., et al. (2020). Evaluation and uncertainty investigation of the NO_2, CO and NH_3 modeling over China under the framework of MICS-Asia III. *Atmospheric Chemistry and Physics*, *20*(1), 181–202. https://doi.org/10.5194/acp-20-181-2020

Kopacz, M., Jacob, D. J., Fisher, J. A., Logan, J. A., Zhang, L., Megretskaia, I. A., et al. (2010). Global estimates of CO sources with high resolution by adjoint inversion of multiple satellite datasets (MOPITT, AIRS, SCIAMACHY, TES). *Atmospheric Chemistry and Physics*, *10*(3), 855–876. https://doi.org/10.5194/acp-10-855-2010

Kurokawa, J., Ohara, T., Morikawa, T., Hanayama, S., Janssens-Maenhout, G., Fukui, T., et al. (2013). Emissions of air pollutants and greenhouse gases over Asian regions during 2000–2008: Regional Emission Inventory in Asia (REAS) version 2. *Atmospheric Chemistry and Physics*, *13*(21), 11019–11058. https://doi.org/10.5194/acp-13-11019-2013

Lai, A. C. K., & Chen, F. Z. (2007). Comparison of a new Eulerian model with a modified Lagrangian approach for particle distribution and deposition indoors. *Atmospheric Environment*, *41*(25), 5249–5256. https://doi.org/10.1016/j.atmosenv.2006.05.088

Li, M., Liu, H., Geng, G., Hong, C., Liu, F., Song, Y., et al. (2017). Anthropogenic emission inventories in China: A review. *National Science Review*, *4*(6), 834–866. https://doi.org/10.1093/nsr/nwx150

Mao, Y., Wang, H., Jiang, F., Feng, S., Jia, M., & Ju, W. (2024). Anthropogenic NO_x emissions of China, the U.S. and Europe from 2019 to 2022 inferred from TROPOMI observations. *Environmental Research Letters*, *19*(5), 054024. https://doi.org/10.1088/1748-9326/ad3cf9

Miyazaki, K., Eskes, H. J., & Sudo, K. (2015). A tropospheric chemistry reanalysis for the years 2005–2012 based on an assimilation of OMI, MLS, TES, and MOPITT satellite data. *Atmospheric Chemistry and Physics*, *15*(14), 8315–8348. https://doi.org/10.5194/acp-15-8315-2015

Müller, J.-F., Stavrakou, T., Bauwens, M., George, M., Hurtmans, D., Coheur, P.-F., et al. (2018). Top-down CO emissions based on IASI observations and Hemispheric constraints on OH levels. *Geophysical Research Letters*, *45*(3), 1621–1629. https://doi.org/10.1002/2017GL076697

National Bureau of Statistics. (2021). National Bureau of statistics. Retrieved from https://www.stats.gov.cn/sj/ndsj. last access: 06/01/2023.

Pan, X. L., Kanaya, Y., Wang, Z. F., Tang, X., Takigawa, M., Pakpong, P., et al. (2014). Using Bayesian optimization method and FLEXPART tracer model to evaluate CO emission in East China in springtime. *Environmental Science & Pollution Research*, *21*(5), 3873–3879. https://doi.org/10.1007/s11356-013-2317-2

Peng, L., Zhang, Q., Yao, Z., Mauzerall, D. L., Kang, S., Du, Z., et al. (2019). Underreported coal in statistics: A survey-based solid fuel consumption and emission inventory for the rural residential sector in China. *Applied Energy*, *235*(FEB.1), 1169–1182. https://doi.org/10.1016/j.apenergy.2018.11.043

Qu, Z., Henze, D. K., Worden, H. M., Jiang, Z., Gaubert, B., Theys, N., & Wang, W. (2022). Sector-based top-downestimates of NO_x, SO_2, and CO emissions in East Asia. *Geophysical Research Letters*, *49*(2), e2021GL096009. https://doi.org/10.1029/2021GL096009

Roemer, M. G. M., & van den Hout, K. D. (1992). Emissions of NMHCS and NOx and global ozone production. In H. vanDop & G. Kallos (Eds.), *Air pollution modeling and its application IX. NATO challenges of modern society* (Vol. 17). Springer. https://doi.org/10.1007/978-1-4615-3052-7_40

Sahu, S. K., Mangaraj, P., Sahoo, P., Mishra, A., & Beig, G. (2024). Quantification and spatial analysis of gridded (0.1°× 0.1°) emission of indirect GHGs/Air pollutants from anthropogenic sources in India. *Environment and Pollution*, *363*, 125231. https://doi.org/10.1016/j.envpol.2024.125231

Saikawa, E., Kim, H., Zhong, M., Avramov, A., Zhao, Y., Janssens-Maenhout, G., et al. (2017). Comparison of emissions inventories of anthropogenic air pollutants and greenhouse gases in China. *Atmospheric Chemistry and Physics*, *17*(10), 6393–6421. https://doi.org/10.5194/acp-17-6393-2017

Sauvage, B., Fontaine, A., Eckhardt, S., Auby, A., Boulanger, D., Petetin, H., et al. (2017). Source attribution using FLEXPART and carbon monoxide emission inventories: SOFT-IO version 1.0. *Atmospheric Chemistry and Physics*, *17*(24), 1–48. https://doi.org/10.5194/acp-17-15271-2017

Seibert, P., & Frank, A. (2004). Source-receptor matrix calculation with a Lagrangian particle dispersion model in backward mode. *Atmospheric Chemistry and Physics*, *4*(1), 51–63. https://doi.org/10.5194/acp-4-51-2004

Seinfeld, J. H., & Pandis, S. N. (2016). *Atmospheric chemistry and physics: From air pollution to climate change*. John Wiley & Sons. https://doi.org/10.1080/00139157.1999.10544295

Shan, Y., Huang, Q., Guan, D., & Hubacek, K. (2020). China CO_2 emission accounts 2016–2017. *Scientific Data*, *7*(1), 54. https://doi.org/10.1038/s41597-020-0393-y

Shi, Q., Zheng, B., Zheng, Y., Tong, D., Liu, Y., Ma, H., et al. (2022). Co-benefits of CO_2 emission reduction from China's clean air actions between 2013–2020. *Nature Communications*, *13*(1), 5061. https://doi.org/10.1038/s41467-022-32656-8

Stein, O., Schultz, M. G., Bouarar, I., Clark, H., Huijnen, V., Gaudel, A., et al. (2014). On the wintertime low bias of Northern Hemisphere carbon monoxide found in global model simulations. *Atmospheric Chemistry and Physics*, *14*(17), 9295–9316. https://doi.org/10.5194/acp-14-9295-2014

Stohl, A. (1998). Computation, accuracy and applications of trajectories-a review and bibliography. *Atmospheric Environment*, *32*(6), 947–966. https://doi.org/10.1016/S1352-2310(97)00457-3

Stohl, A. (2006). Characteristics of atmospheric transport into the Arctic troposphere. *Journal of Geophysical Research*, *111*(D11), D11306. https://doi.org/10.1029/2005jd006888

Stohl, A., Forster, C., Eckhardt, S., Spichtinger, N., Huntrieser, H., Heland, J., et al. (2003). A backward modeling study of intercontinental pollution transport using aircraft measurements. *Journal of Geophysical Research*, *108*(D12), 4370. https://doi.org/10.1029/2002JD002862

Streets, D. G., Canty, T., Carmichael, G. R., de Foy, B., Dickerson, R. R., Duncan, B. N., et al. (2013). Emissions estimation from satellite retrievals: A review of current capability. *Atmospheric Environment*, *77*, 1011–1042. https://doi.org/10.1016/j.atmosenv.2013.05.051

Tanimoto, H., Sawa, Y., Yonemura, S., Yumimoto, K., Matsueda, H., Uno, I., et al. (2008). Diagnosing recent CO emissions and ozone evolution in East Asia using coordinated surface observations, adjoint inverse modeling, and MOPITT satellite data. *Atmospheric Chemistry and Physics*, *8*(14), 3867–3880. https://doi.org/10.5194/acp-8-3867-2008

Thompson, R., Patra, P., Chevallier, F., Maksyutov, S., Law, R. M., Ziehn, T., et al. (2016). Top-down assessment of the Asian carbon budget since the mid 1990s. *Nature Communications*, *7*(1), 10724. https://doi.org/10.1038/ncomms10724

Thompson, R. L., Sasakawa, M., Machida, T., Aalto, T., Worthy, D., Lavric, J. V., et al. (2017). Methane fluxes in the high northern latitudes for 2005–2013 estimated using a Bayesian atmospheric inversion. *Atmospheric Chemistry and Physics*, *17*(5), 3553–3572. https://doi.org/10.5194/acp-17-3553-2017

Thompson, R. L., & Stohl, A. (2014). FLEXINVERT: An atmospheric Bayesian inversion framework for determining surface fluxes of trace species using an optimized grid. *Geoscientific Model Development*, *7*(5), 2223–2242. https://doi.org/10.5194/gmd-7-2223-2014

Thompson, R. L., Stohl, A., Zhou, L. X., Dlugokencky, E., Fukuyama, Y., Tohjima, Y., et al. (2015). Methane emissions in East Asia for 2000–2011 estimated using an atmospheric Bayesian inversion. *Journal of Geophysical Research: Atmospheres*, *120*(9), 4352–4369. https://doi.org/10.1002/2014JD022394

van der Werf, G. R., Randerson, J. T., Giglio, L., van Leeuwen, T. T., Chen, Y., Rogers, B. M., et al. (2017). Global fire emissions estimates during 1997–2016. *Earth System Science Data*, *9*(2), 697–720. https://doi.org/10.5194/essd-9-697-2017

Wang, R., Tao, S., Balkanski, Y., Ciais, P., Boucher, O., Liu, J., et al. (2014). Exposure to ambient black carbon derived from a unique inventory and high-resolution model. *Proceedings of the National Academy of Sciences*, *111*(7), 2459–2463. https://doi.org/10.1073/pnas.1318763111

Worden, H. M., Deeter, M. N., Frankenberg, C., George, M., Nichitiu, F., Worden, J., et al. (2013). Decadal record of satellite carbon monoxide observations. *Atmospheric Chemistry and Physics*, *13*(2), 837–850. https://doi.org/10.5194/acp-13-837-2013

Yin, Y., Chevallier, F., Ciais, P., Broquet, G., Fortems-Cheiney, A., Pison, I., & Saunois, M. (2015). Decadal trends in global CO emissions as seen by MOPITT. *Atmospheric Chemistry and Physics*, *15*(23), 13433–13451. https://doi.org/10.5194/acp-15-13433-2015

Yumimoto, K., Uno, I., & Itahashi, S. (2014). Long-term inverse modeling of Chinese CO emission from satellite observations. *Environment and Pollution*, *195*, 308–318. https://doi.org/10.1016/j.envpol.2014.07.026

Zhang, Q., Streets, D. G., Carmichael, G. R., He, K. B., Huo, H., Kannari, A., et al. (2009). Asian emissions in 2006 for the NASA INTEX-B mission. *Atmospheric Chemistry and Physics*, *9*(14), 5131–5153. https://doi.org/10.5194/acp-9-5131-2009

Zhao, Y., Zhang, J., & Nielsen, C. P. (2013). The effects of recent control policies on trends in emissions of anthropogenic atmospheric pollutants and CO_2 in China. *Atmospheric Chemistry and Physics*, *13*(2), 487–508. https://doi.org/10.5194/acp-13-487-2013

Zheng, B., Chevallier, F., Yin, Y., Ciais, P., Fortems-Cheiney, A., Deeter, N. M., et al. (2019). Global atmospheric carbon monoxide budget 2000–2017 inferred from multi-species atmospheric inversions. *Earth System Science Data*, *11*(3), 1411–1436. https://doi.org/10.5194/essd-11-1411-2019

Zheng, B., Tong, D., Li, M., Liu, F., Hong, C., Geng, G., et al. (2018). Trends in China's anthropogenic emissions since 2010 as the consequence of clean air actions. *Atmospheric Chemistry and Physics*, *18*(19), 14095–14111. https://doi.org/10.5194/acp-18-14095-2018

Zhong, Q. R., Huang, Y., Shen, H. Z., Chen, Y. L., Chen, H., Huang, T. B., et al. (2017). Global estimates of carbon monoxide emissions from 1960 to 2013. *Environmental Science & Pollution Research*, *24*(1), 864–873. https://doi.org/10.1007/s11356-016-7896-2

Zhou, Y., Xing, X., Lang, J., Chen, D., Cheng, S., Wei, L., et al. (2017). A comprehensive biomass burning emission inventory with high spatial and temporal resolution in China. *Atmospheric Chemistry and Physics*, *17*(4), 2839–2864. https://doi.org/10.5194/acp-17-2839-2017